ELSEVIER

Earth and Planetary Science Letters 206 (2003) 335–348

EPSL

www.elsevier.com/locate/epsl

# Lagrangian structures and stirring in the Earth's mantle

Cinzia G. Farnetani *, Henri Samuel

*Laboratoire de Dynamique des Systèmes Géologiques, Institut de Physique du Globe de Paris, Paris, France*

Received 24 July 2002; received in revised form 14 November 2002; accepted 15 November 2002

**Abstract**

In this paper we investigate three Lagrangian methods that have been recently proposed to quantify mixing in chaotic and time-aperiodic geophysical flows. The analytical method proposed by Haller [e.g., G. Haller, Chaos 10 (2000) 99–108] has a strong mathematical foundation and seeks to determine the location of stable (i.e., most attracting) and unstable (i.e., most repelling) material lines. The main hyperbolic lines describe the spatial organization of chaotic mixing. The finite-size Lyapunov exponents estimate the local mixing properties of the flow using the finite dispersion of particles, while the finite-time Lyapunov exponents have been often used to locate dynamically distinguished regions in geophysical flows. Mantle stirring is induced by the repeated action of stretching and folding, thus requiring to follow the strain history of a fluid element along a trajectory. We calculate the trajectories of more than half a million passive tracers forward and backward in time. The Eulerian velocity field is computed using a finite element code for solid state convection. We focus on a thermochemical model with a chemically denser layer at the base of the Earth's mantle. This case allows us to test the ability of the Lagrangian techniques to detect the location of a dynamical barrier that inhibits mass exchanges and delimits domains characterized by different efficiency of stirring. We find that the Lagrangian techniques provide a satisfactory description of the main structures governing stirring, and enlighten different and complementary aspects: the methods based on the Lyapunov exponents provide a clear picture of mantle domains characterized by different strength of stirring, while the method proposed by Haller identifies the skeleton of the main structures around which stirring is organized. Our paper builds toward a more rigorous analysis of the stirring processes in the Earth's mantle, which is required to understand the existence of geochemical reservoirs under a dynamical prospective.


*Keywords:* Lagrangian coherent structures; Lyapunov exponent; stirring; mixing; mantle convection

## 1. Introduction

The understanding of convective mixing is fundamental for the interpretation of geochemical heterogeneities observed in surface rocks. Pioneering papers by Hoffman and McKenzie [1] and by Gurnis and Davies [2] attempted to determine the mixing time scales in the Earth's mantle. The estimated 'lifetime' of heterogeneities diverged widely, ranging from 0.5–1 Ga [1] to 1–2 Ga [2] or more, in such case implying the possible survival of primitive mantle [3]. Christensen [4] shed light on the problem by identifying that for kine-

* Corresponding author.
*E-mail address:* cinzia@ipgp.jussieu.fr (C.G. Farnetani).

0012-821X/02/$ – see front matter © 2002 Elsevier Science B.V. All rights reserved.
doi:10.1016/S0012-821X(02)01085-3

matic models poorly mixed 'islands' of material may survive, while for consistent dynamical models the size of the heterogeneities always decreases exponentially with time, leading to efficient mixing. Further studies in two dimensions (for a review see [5]) quantified mixing rates by using infinitesimal elliptical strain markers and by monitoring the progressive dispersal of passive tracers. More recent studies in three dimensions [6] use Lyapunov exponents and Poincaré maps to describe stirring induced by a time-periodic, kinematic flow.

Although these models improved our knowledge of mantle mixing we still lack a thorough understanding of the dynamical processes leading to the existence of geochemical heterogeneities in the Earth's mantle. A widely accepted way to interpret the geochemical signature of surface lavas is to invoke variable degrees of mixing of distinct geochemical reservoirs. In the last 20 years several geochemical end-members have been defined [7] based on the isotopic ratios of Sr, Nd and Pb. From a geochemical stand point it is possible to explain a large range of observed isotope ratios by invoking only four distinct reservoirs [8]. However, some isotopic systems such as helium require to postulate the existence of another reservoir with high $^{3}He/^{4}He$ [9].

The existence of geochemical reservoirs should also be investigated under a dynamical prospective to understand: (1) How is it possible to generate and preserve distinct reservoirs in a vigorously convective mantle? (2) What dynamical processes govern the mass exchange between reservoirs, in other words, how does mixing between reservoirs actually occur? (3) Are the reservoirs geochemically distinct since they experienced a distinct dynamical evolution? A necessary prerequisite to address such questions is a thorough understanding of mantle stirring.

In this paper we compare recent algorithms that have been used to quantify transport and mixing of geophysical fluids. For example they have been applied: (i) to the atmospheric flows, to investigate the dynamics of the stratospheric polar vortex [10,11], (ii) to the oceanic flows to analyze fluid particle paths of the Gulf Stream [12], and (iii) to laboratory experiments of fluid mixing [13]. However, to our knowledge, they have never been applied to the flow of Earth's mantle.

One of the most challenging aspects of real geophysical flows is that they are time-aperiodic. Poincaré maps provide a useful tool for identifying chaotic zones in flows with a periodic or quasi-periodic time dependence [14]. However, they cannot be applied to flows with a general time dependence. It is only recently that theoretical work [15–17] has been developed to describe the transport and mixing behavior of a chaotic and aperiodic fluid flow.

Two approaches can be used to define the coherent structures in two-dimensional turbulent fluid flows (for a review see [16], and references therein). The Eulerian approach is based on the instantaneous distribution of a scalar field, such as vorticity, kinetic energy and strain. The Lagrangian approach is based on the advection of passive tracers, which allows to identify regions displaying different dynamical behavior. An initially circular blob of passive tracers will reveal the Lagrangian coherent structures through stretching, thinning and folding around them. The objective of this approach is to determine the nature of the Lagrangian coherent structures, and to study their location and interaction.

In this paper we consider only the Lagrangian approach and we investigate (1) the method proposed by Haller [15,16], thereafter called the hyperbolic persistence time method, which enables to identify stable and unstable material lines, (2) the method based on the finite-size Lyapunov exponents, (3) the method based on the finite-time Lyapunov exponents. We calculate the flow field for solid state convection in the Earth's mantle using a two-dimensional finite element code in Cartesian geometry. This is an obvious limitation that does not allow us to catch the complexity of a fully three-dimensional flow, however some Lagrangian techniques become technically challenging in 3-D. For example, 10 different categories of attracting and repelling material surfaces should be identified in 3-D [18], as opposed to only two categories in 2-D.

Our main interest here is to understand the ability of different Lagrangian techniques to cap-

ture the location of barrier regions and of stirring regions, and to quantify the strength of stirring.

## 2. Convection model

The code for solid state convection of a Newtonian, incompressible viscous fluid at infinite Prandtl number [19] solves the non-dimensional equations using the Boussinesq approximation:

conservation of mass:

$$\nabla \cdot u = 0, \tag{1}$$

conservation of momentum:

$$\Delta u = -\nabla p - \mathrm{Ra}\,\theta \vec{z}, \tag{2}$$

conservation of energy:

$$\frac{\partial \theta}{\partial t} + u \cdot \nabla \theta = \Delta \theta + H \tag{3}$$

where $u$ is the velocity vector, $\theta$ is the potential temperature, $t$ is time, $p$ the dynamic pressure, $H$ is the internal heating, Ra is the Rayleigh number and $\vec{z}$ is a unit vector in the vertical direction. The equations are non-dimensionalized by scaling distance over the box depth $D$, temperature according to the temperature contrast between the top and the bottom surfaces $\Delta\theta$, time according to $D^2/\kappa$, and the internal heating to $\rho D^2/k\Delta\theta$. Numerical values of the scaling parameters are given in Table 1.

The thermal expansion coefficient is depth dependent and varies from $5\times10^{-5}$ K$^{-1}$ at the surface to $1\times10^{-5}$ K$^{-1}$ at the bottom of the box. The equation used is $\alpha(z) = \exp(Ah)$, where $h$ is non-dimensional height above the bottom of the box and $A = 1.61$ is a constant chosen to best reproduce experimental data [20]. The viscosity is reduced one order of magnitude from 100 km depth to 660 km depth, in order to simulate a relatively low viscosity upper mantle ($\eta_{\mathrm{um}} = 8\times10^{20}$ Pa s).

Using the physical parameters given in Table 1 the Rayleigh number is:

$$\mathrm{Ra} = \frac{g\rho\alpha_s\Delta\theta D^3}{\kappa\eta} = 1.7\times10^7. \tag{4}$$

The size of our domain in the $X$ and $Z$ directions is $8700\times2900$ km. It is meshed by $435\times145$ elements, providing a constant element size of 20 km/element.

At the top and bottom surfaces we impose zero vertical velocity and horizontal free slip ($u_z = 0 = \partial u_x/\partial z$). The boundary condition for the temperature field is constant ($\theta_{\mathrm{top}} = 0$ and $\theta_{\mathrm{bottom}} = 1$). At the side walls we impose periodic boundary conditions.

We conducted a purely thermal convection calculation and a thermochemical convection calculation. The latter is actually a very interesting test case to assess the ability of the Lagrangian techniques to detect regions characterized by different transport and stirring properties. In the case of thermochemical convection we introduce two families of active tracers: one to simulate the subducted oceanic crust (10 km thick), which is considered to be 3% denser than the surrounding mantle, and a second one to simulate a layer of denser material at the base of the Earth's mantle.

Table 1
Physical parameters

| Symbol | Parameter | Value | Unit |
|---|---|---|---|
| $D$ | mantle depth | $2900\times10^3$ | m |
| $\Delta\theta$ | temperature contrast | 2800 | K |
| $g$ | gravitational acceleration | 10 | m s$^{-2}$ |
| $\rho$ | mantle density | 4000 | kg m$^{-3}$ |
| $\eta$ | mantle viscosity | $8\times10^{21}$ | Pa s |
| $\alpha_s$ | surface thermal expansion coefficient | $5\times10^{-5}$ | K$^{-1}$ |
| $\kappa$ | thermal diffusivity | $10^{-6}$ | m$^2$ s$^{-1}$ |
| $k$ | thermal conductivity | 4.8 | W m$^{-1}$ K$^{-1}$ |
| $H$ | dimensional internal heating | $8.0\times10^{-12}$ | W kg$^{-1}$ |

Such layer occupies an initial volume corresponding to 20% of the whole mantle volume and it is 1.8% chemically denser than the overlying mantle. The buoyancy number $B$ for the layer is the chemical density contrast over the thermal density contrast:

$$B = \frac{\Delta\rho_{\mathrm{ch}}}{\rho\alpha_{\mathrm{layer}}\Delta\theta} = 0.6. \quad (5)$$

For thermochemical convection the buoyancy force in the right-hand side of Eq. 2 is modified to include the effect of active tracers present at each time step in each element (for more details see [21]). Since we use 16 active tracers per element, more than $2\times10^5$ tracers are used to follow the evolution of the dense layer. The number of crustal tracers increases with time, since we consider that new oceanic crust is continuously formed at divergent zones. A careful description of the method used to insert and to advect active tracers is given in [21], where we also provide the results of a benchmarking for thermochemical convection.

## 3. Transport calculations for Lagrangian methods

Stirring involves the repeated action of stretching and folding of a fluid element, while mixing also involves diffusion at small scales [14]. The term stirring is more appropriate for the mantle, since rocks chemical diffusivity is only $10^{-15}$–$10^{-20}$ m$^2$ s$^{-1}$.

The Lagrangian methods used to describe stirring require to advect passive tracers forward in time (from time $t_0$ to $t_{0+\Delta T}$, where $\Delta T$ is a given time interval) and backward in time (from time $t_0$ to $t_{0-\Delta T}$). Transport calculations are performed as a post processing, using the velocity field saved at each time step and for each node of the grid. The advection is performed using a second-order Runge–Kutta method for the time scheme and the two-dimensional bicubic spline interpolation scheme by Akima [22], which minimizes spurious over- and under-shoots better than a cubic spline [10]. Passive tracers are distributed regularly in each grid element, since we generally use nine tracers per element, more than half a million trajectories are calculated forward and backward in time.

### 3.1. Hyperbolic persistence time method

A material line is called unstable (or repelling) if in a given time interval, forward in time, all nearby fluid trajectories separate from it. A material line is called stable (or attracting) if in a given time interval, backward in time, all nearby fluid trajectories separate from it. The location of the attracting and repelling material lines is used to define the boundaries of the coherent structures of the flow.

Haller [15] has derived an analytical method to locate attracting and repelling finite-time hyperbolic material lines for two-dimensional, non-periodic, time-dependent velocity fields. Note that the unstable and stable hyperbolic material lines are the finite-time generalizations of the stable and unstable hyperbolic manifolds[1], respectively, which they approach as time goes to infinity [10].

Following [15] we calculate at each time $t$ and for each advected tracer located in $\boldsymbol{x}(t)$ the determinant of the velocity gradient tensor:

$$D_x u(\boldsymbol{x}(t), t) = \begin{bmatrix} \frac{\partial u_x}{\partial x} & \frac{\partial u_x}{\partial z} \\ \frac{\partial u_z}{\partial x} & \frac{\partial u_z}{\partial z} \end{bmatrix} \quad (6)$$

The sign of the determinant characterizes the flow in the neighborhood of each particle: the flow is separated into elliptic regions (if $\det D_x u > 0$), in parabolic regions (if $\det D_x u = 0$) and in hyperbolic regions (if $\det D_x u < 0$). Elliptic regions represent an obstacle to efficient stirring, since they translate and rotate conserving their identity [23], while hyperbolic regions represent the main skeleton governing large-scale stirring. In other words, the main hyperbolic lines (i.e., the material lines that are locally the most attracting or repelling) describe the spatial organization of chaotic stirring.

[1] It is easy to see that the stable manifold of a hyperbolic point is repelling all nearby trajectories.

We should remark that Okubo and Weiss (e.g., [24]) have been the first ones to recognize the significance of the determinant of the velocity gradient tensor and to propose the elliptic–hyperbolic partition, albeit for a flow constant with time.

For each tracer trajectory we calculate the time period over which the determinant of the velocity gradient tensor is strictly negative. Tracers that exhibit $\det D_x u < 0$ for long time are on, or asymptotic to a uniformly finite-time hyperbolic trajectory. We calculate the local maxima of hyperbolic persistence defined for forward integration as:

$$d_T^+(\boldsymbol{x}_0, t_0) = \max\{(t-t_0) \,|\, \det D_x u(\boldsymbol{x}(\tau, \boldsymbol{x}_0), \tau) < 0\}$$
$$\text{for } t \in [t_0, t_0 + \Delta T] \text{ and } t_0 \leq \tau < t \tag{7}$$

Local repelling material lines can be obtained by forward advection, while local attracting material lines are obtained by backward advection, once again by requiring $\det D_x u < 0$:

$$d_T^-(\boldsymbol{x}_0, t_0) = \max\{(t_0-t) \,|\, \det D_x u(\boldsymbol{x}(\tau, \boldsymbol{x}_0), \tau) < 0\}$$
$$\text{for } t \in [t_0-\Delta T, t_0] \text{ and } t < \tau \leq t_0 \tag{8}$$

The local maxima of $d_T^+$ and $d_T^-$ are respectively mapping the repelling and attracting material lines which intersect at the hyperbolic points [15].

Haller's first condition, explained above, simply requires to calculate the time interval during which the determinant of the velocity gradient tensor, for each tracer trajectory, is negative. Haller [15] has a second condition on the rotation of the Eulerian eigenvectors. The additional condition is explained in the Appendix but is not used throughout the paper, since we find that by including it the results become more difficult to interpret. Such lack of improvement may be due to various reasons: (i) in our flow the coherent structures do not change very rapidly with time, (ii) the second condition is particularly sensitive to small numerical errors, thus the results may look worse for numerical reasons (Haller, personal communication). Therefore, although the second condition should be in principle evaluated, whether or not it will improve the results depends on the specific type of flow and on the resolution.

Lapeyre et al. [25] propose to non-dimensionalize the calculated hyperbolic persistence time by the strain rate. To do this we calculate the eigenvalues $\lambda$ of the strain rate tensor:

$$\dot{\varepsilon}_{ij} = \frac{1}{2}\left(\frac{\partial u_i}{\partial x_j} + \frac{\partial u_j}{\partial x_i}\right). \tag{9}$$

Using the incompressibility Eq. 1 we find the eigenvalue $\lambda$ for each tracer, which is then used to non-dimensionalize the hyperbolic persistence time $d_T^+$ and $d_T^-$ calculated above.

### 3.2. Finite-size Lyapunov exponents

This method estimates the local stirring properties of the flow using the finite dispersion of particles [10,11,26]. Consider a pair of particles at an initial distance $\delta_0$ at time $t$ and at initial location $\boldsymbol{x}$ thus: $\delta(\boldsymbol{x},t,0) = \delta_0$. We want to find the time $\tau$ required to increase the separation between the two particles by a growth factor $\gamma$, so that at time $t+\tau$ the separation is: $\delta(\boldsymbol{x},t,\tau) = \gamma\delta_0$.

The finite-size Lyapunov exponent is then defined as:

$$\lambda_\gamma(\boldsymbol{x}, t, \delta_0) = \frac{1}{\tau} \ln \gamma \tag{10}$$

We advect more than $2.5 \times 10^5$ passive tracers forward and backward in time over a finite-time interval $\Delta T$. At each time step we calculate the distance between each tracer and its four neighboring tracers, initially equally spaced in the four cardinal directions. We keep track of the elapsed time $\tau$ at which the distance between each tracer and its four neighboring tracers becomes greater than the predefined threshold distance ($\gamma\delta_0$). We then calculate the finite-size Lyapunov exponent (FSLE) of the tracer using the equation given above. The FSLE of a tracer is set to zero if the threshold distance is not reached during the finite-time interval considered.

### 3.3. Finite-time Lyapunov exponents

Finite-time Lyapunov exponents have been employed to locate dynamically distinguished regions in geophysical flow data [27], in kinematic mantle convection models [6] and to study deformations in mantle plumes [28]. The Lyapunov exponents are a convenient indicator of the sensitivity to

small perturbations of the initial position and provide the exponential rate of divergence of infinitesimally nearby initial trajectories.

To calculate the finite-time Lyapunov exponents we consider a trajectory starting at the position $x_0$ at time $t_0$ and ending at the position $x_1$ at time $t_1$. The infinitesimal displacement $\boldsymbol{\xi}_0$ at time $t_0$ is transformed into $\boldsymbol{\xi}_1$ at time $t_1$ by:

$$\boldsymbol{\xi}_1 = \boldsymbol{M}(x_0, t_0; x_1, t_1)\boldsymbol{\xi}_0, \tag{11}$$

where $\boldsymbol{M}$ is a linear operator given by the integration of:

$$\frac{\mathrm{d}\boldsymbol{M}}{\mathrm{d}t} = D_x u(\boldsymbol{x}(t), t)\boldsymbol{M} \tag{12}$$

along the trajectory, where $D_x u(\boldsymbol{x}(t),t)$ is the velocity gradient evaluated along the trajectory. At the initial time $t_0$ the matrix $\boldsymbol{M}$ corresponds to the identity matrix.

The variation of the displacement over the interval $[t_0,t_1]$ is given by the ratio:

$$\frac{|\boldsymbol{\xi}_1|}{|\boldsymbol{\xi}_0|} = \frac{|\boldsymbol{M}\boldsymbol{\xi}_0|}{|\boldsymbol{\xi}_0|} = \left(\frac{\boldsymbol{\xi}_0^{\mathrm{T}}\boldsymbol{M}^{\mathrm{T}}\boldsymbol{M}\boldsymbol{\xi}_0}{\boldsymbol{\xi}_0^{\mathrm{T}}\boldsymbol{\xi}_0}\right)^{1/2} \tag{13}$$

This ratio is governed by the real eigenvalues $\sigma_+$ and $\sigma_-$ of $\boldsymbol{M}^{\mathrm{T}}\boldsymbol{M}$, the right Cauchy–Green strain tensor [14] and the projection of $\boldsymbol{\xi}_0$ onto its eigenvectors.

An infinitesimal circular blob of tracers with a non-dimensionalized unit radius, surrounding $x_0$ at time $t_0$ is turned into an ellipsoid surrounding $x_1$ at time $t_1$ with semi-axes of lengths $\sigma_+$ and $\sigma_-$. Conversely, an infinitesimal circular blob of tracers with a non-dimensionalized unit radius, surrounding $x_1$ at time $t_1$ was an ellipsoid with axes $1/\sigma_+$ and $1/\sigma_-$ surrounding $x_0$ at time $t_0$.

The finite-time Lyapunov exponents or finite-time deformations are defined as:

$$\lambda_+ = \frac{1}{t_1 - t_0}\ln\,\sigma_+,\ \lambda_- = \frac{1}{t_1 - t_0}\ln\,\sigma_-, \tag{14}$$

and are calculated by numerical integration of Eq. 12.

## 4. Results

The objective of this study is to test the ability of different Lagrangian techniques to detect the main structures governing the stirring properties of the flow. Therefore, the convection calculations are used only to provide a velocity field for a chaotic and aperiodic flow. It is out of the purpose of this paper to represent a realistic mantle flow, which would require a fully three-dimensional spherical model with strongly temperature-dependent viscosity and surface plates.

Under these restrictive conditions we can use a fairly simple convection model and we consider its evolution for a limited time interval compared with the age of the Earth. We let the convection code run form an initial linear temperature profile to steady state. This temperature field represents the initial condition for the thermochemical convection calculation, which is then conducted over a time interval of 1500 Myr. We show the results of the thermochemical convection model only at two time periods: after 500 Myr (thereafter called 'early stage') and after 1500 Myr (thereafter called 'late stage')[2]

Fig. 1a shows the temperature and the velocity field for the early stage. Convection is organized in two separate domains: the denser basal layer gradually heats up, due to the bottom heating, and convects internally. Convection in the overlying mantle is organized around cold subducting slabs. Fig. 1b shows the location of tracers used to model the denser layer, different colors represent the initial depth of the tracers. We see that plumes form inside the layer and contribute to the internal stirring. Only a small fraction (1.5%) of denser material is entrained by viscous coupling, forming narrow filaments into rising plumes. Fig. 1c shows the active tracers representing the subducted oceanic crust which sinks to the top of the denser layer.

At the late stage we see more prominent hot plumes rising from the dense layer (Fig. 1d), entraining denser material (Fig. 1e). 21% of the basal tracers have escaped the dense layer, showing that the density stratification acts as a partial barrier to mass exchange. Fig. 1f shows also that

[2] Find the complete set of results at http://www.ipgp.jussieu.fr/~cinzia/EPSL2003.

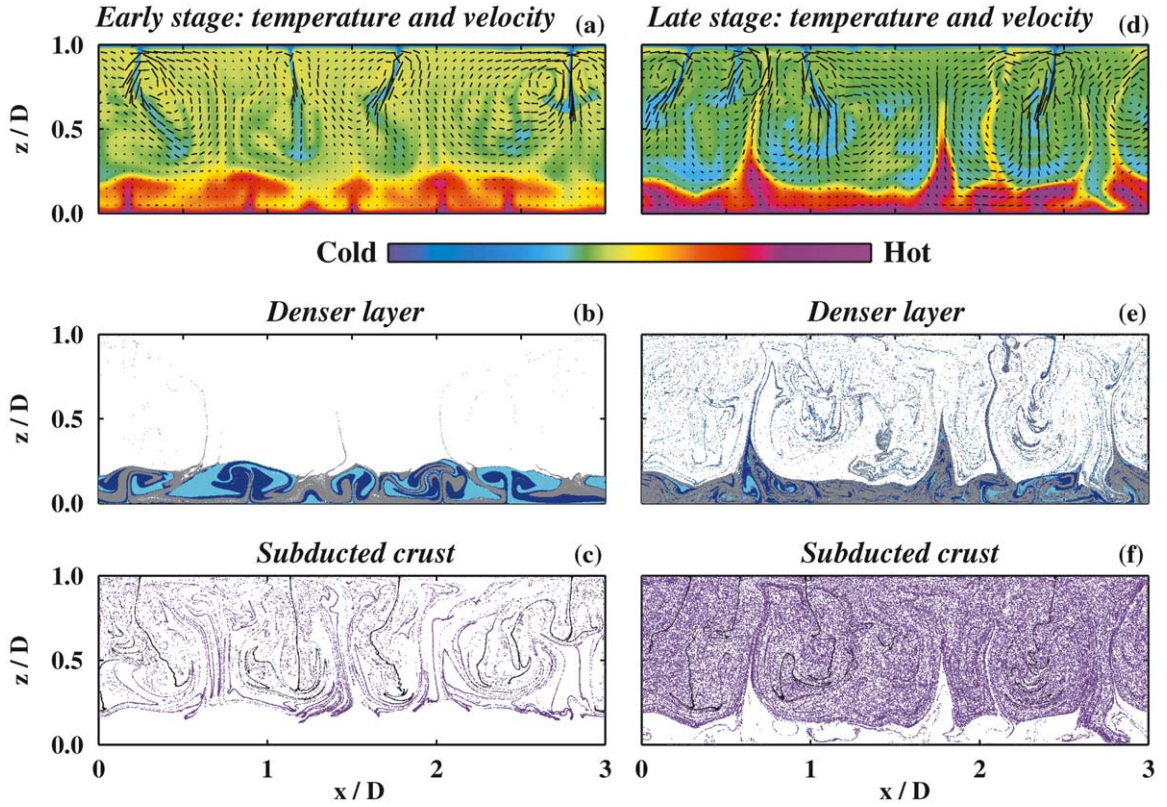


Fig. 1. Left: early stage (i.e., after 500 Myr). Right: late stage (i.e., after 1500 Myr). (a, d) Temperature and velocity fields. (b, e) Active tracers for the denser layer. Colors represent the initial height above the bottom: from 0 to 193 km (cylan), 193–386 km (blue), 386–579 km (gray). (c, f) Tracers for the subducted crust. Subducted crust younger than 150 Myr is indicated in black.

subducted crust may occasionally deflect the denser layer and sink into it.

Finally, we remark that a careful inspection of the velocity field shows a different behavior between the low viscosity upper mantle and the underlying lower mantle. For example, at the late stage the rms of the vertical velocity component is: 2.0 cm/yr in the upper mantle, 1.6 cm/yr in the lower mantle above the denser layer and 0.2 cm/yr inside the denser layer.

### 4.1. Hyperbolic persistence time method

When applying the hyperbolic persistence time method we need to define the finite-time interval $\Delta T$ for forward and backward advection, but unfortunately there is no clear rule to establish it. For the early stage we have tested three finite-time intervals in order to find empirically the most appropriate $\Delta T$ for our flow. Fig. 2 shows the initial location of passive tracers satisfying $\det D_x u < 0$ during the whole time interval $\Delta T$ of forward advection. For $\Delta T = 40$ Myr (Fig. 2a) large zones of the domain satisfy $\det D_x u < 0$ and it is difficult to sort out the main structure affecting stirring. For $\Delta T = 80$ Myr (Fig. 2b) fewer tracers satisfy $\det D_x u < 0$, in particular tracers initially close to the interface between the dense layer and the overlying mantle persist with $\det D_x u < 0$. Finally, for $\Delta T = 150$ Myr (Fig. 2c) the remaining tracers seem to better locate the interface between the two flow domains and the more persistent subduction zones. For longer time intervals (not shown) the number of tracers may be severely reduced, making the results difficult to interpret. Therefore, although the choice of the time interval

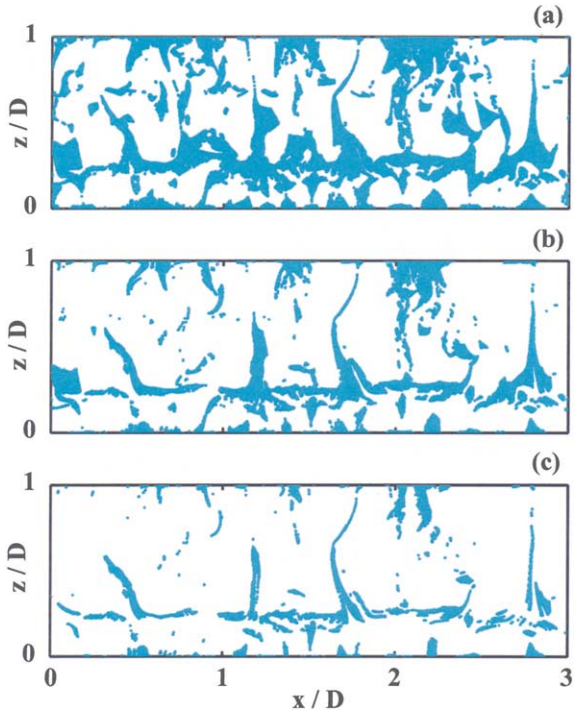


Fig. 2. Hyperbolic persistence time method: Initial location of tracers which have $\det D_x u < 0$ over the entire time interval $\Delta T$ of forward integration. (a) $\Delta T = 40$ Myr, (b) $\Delta T = 80$ Myr, (c) $\Delta T = 150$ Myr. For temperature and velocity field see Fig. 1a.

is arbitrary, from now on we will consider a finite-time interval $\Delta T = 150$ Myr. Given the rms of the vertical velocity component given above this time corresponds to a vertical motion of 2400 km.

Fig. 3 shows the results of forward and backward advection over $\Delta T = 150$ Myr. For the early stage we see that the method captures fairly well the location of the boundary between the dense layer and the overlying mantle, in both forward (Fig. 3a) and backward advection (Fig. 3b). The dominant features emerging from forward advection correspond to the zones where the descending flow, associated to the slabs, impinges on the denser layer. The flow is here diverging and we clearly identify the unstable (or repelling) material lines. The dominant features emerging from backward advection correspond to the main upwelling zones located just above the dense layer. It is useful to remind that plumes would correspond to diverging flow, when integrated backward in time. In other words backward advection shows the location of stable (or attracting) material lines. Flow regions dominated by subduction often show high strain rate-normalized hyperbolic persistence time. For the late stage (Fig. 3c and d) the method still captures the main features of the flow, although the interface between the dense layer and the overlying mantle is less clear. This

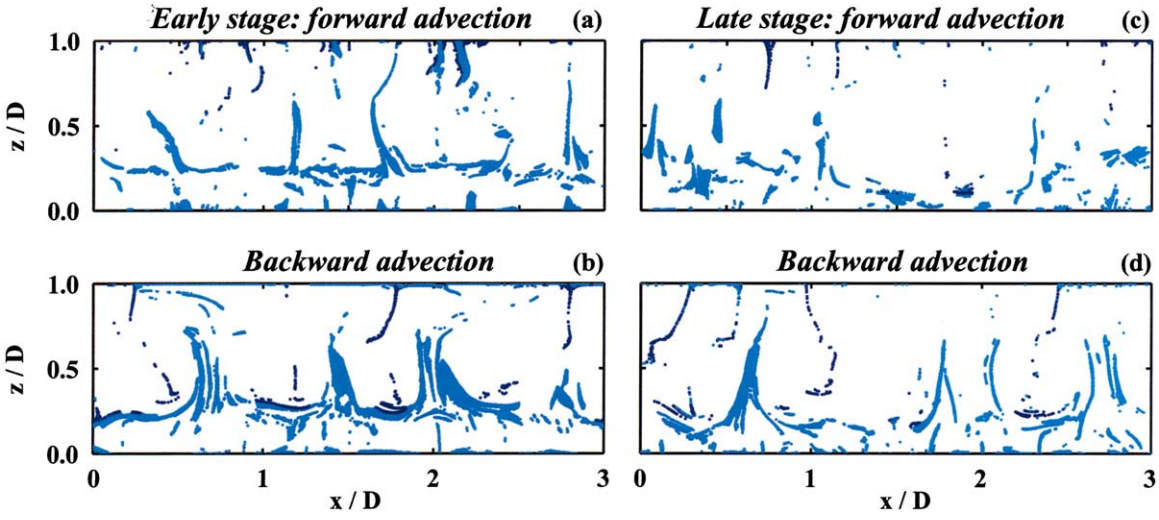


Fig. 3. Hyperbolic persistence time method: Initial location of tracers which have $\det D_x u < 0$ over the entire time interval $\Delta T = 150$ Myr. Early stage: (a) forward integration, (b) backward integration. Late stage: (c) forward integration, (d) backward integration. Tracers with high strain rate-normalized persistence time are in dark blue.

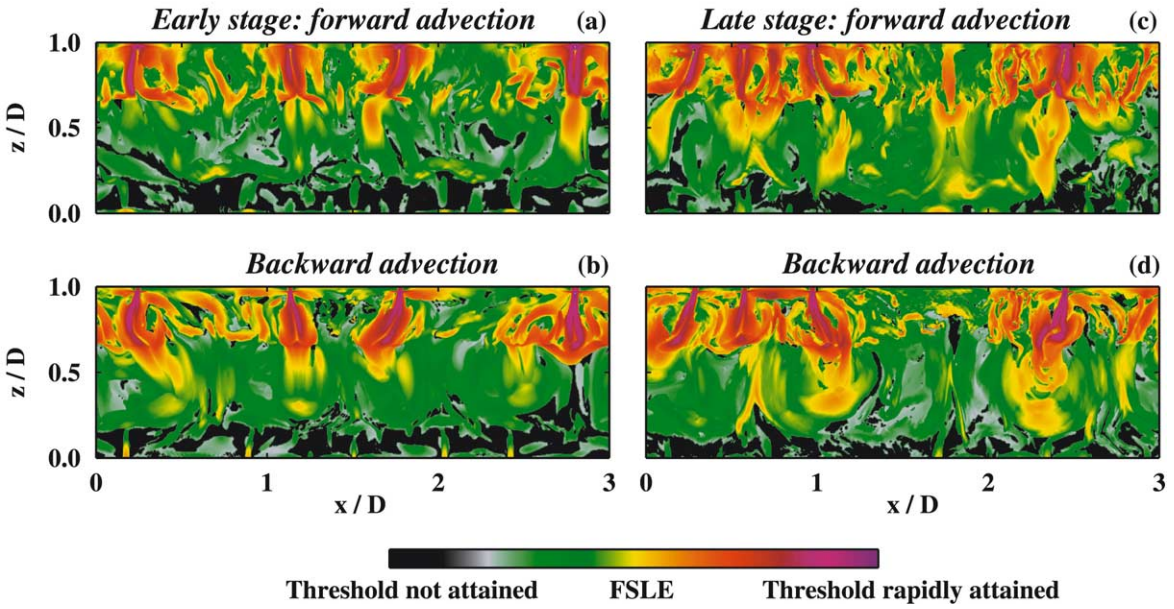


Fig. 4. Finite-size Lyapunov exponents. Early stage: (a) forward integration, (b) backward integration. Late stage: (c) forward integration, (d) backward integration. Tracers are in their initial location.

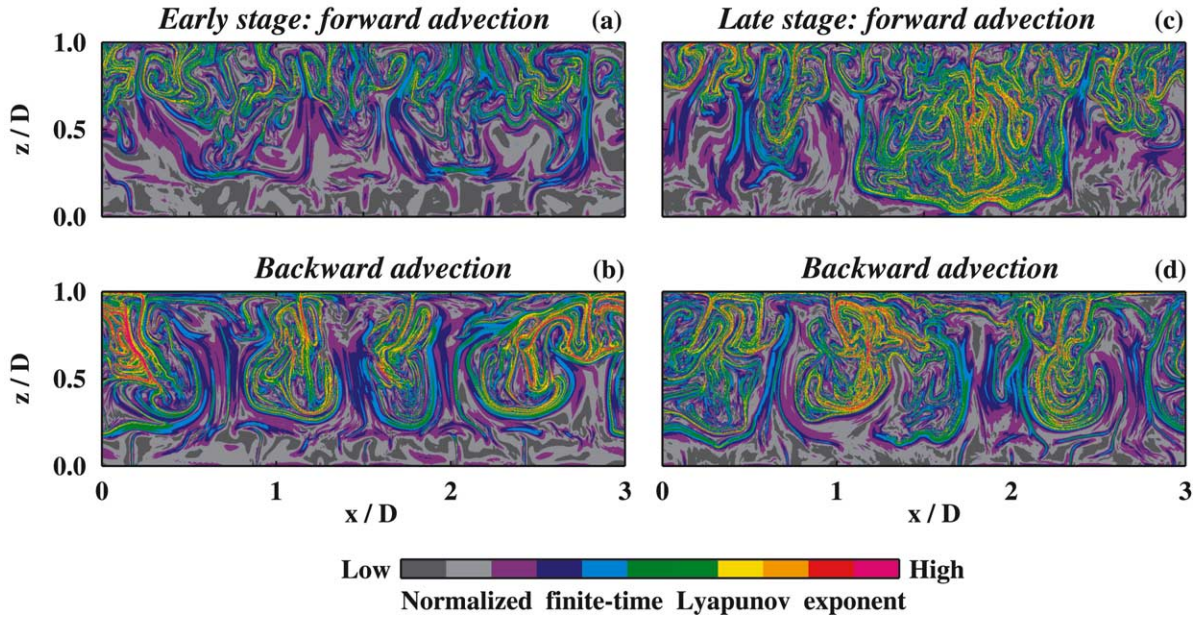


Fig. 5. Finite-time Lyapunov exponents. Early stage: (a) forward integration, (b) backward integration. Late stage: (c) forward integration, (d) backward integration. Tracers are in their initial location. For graphical purpose values are normalized over the maximum value $FTLE_{max}$ and the color scale is saturated (i.e., all $FTLE > 0.5FTLE_{max}$ are in magenta).

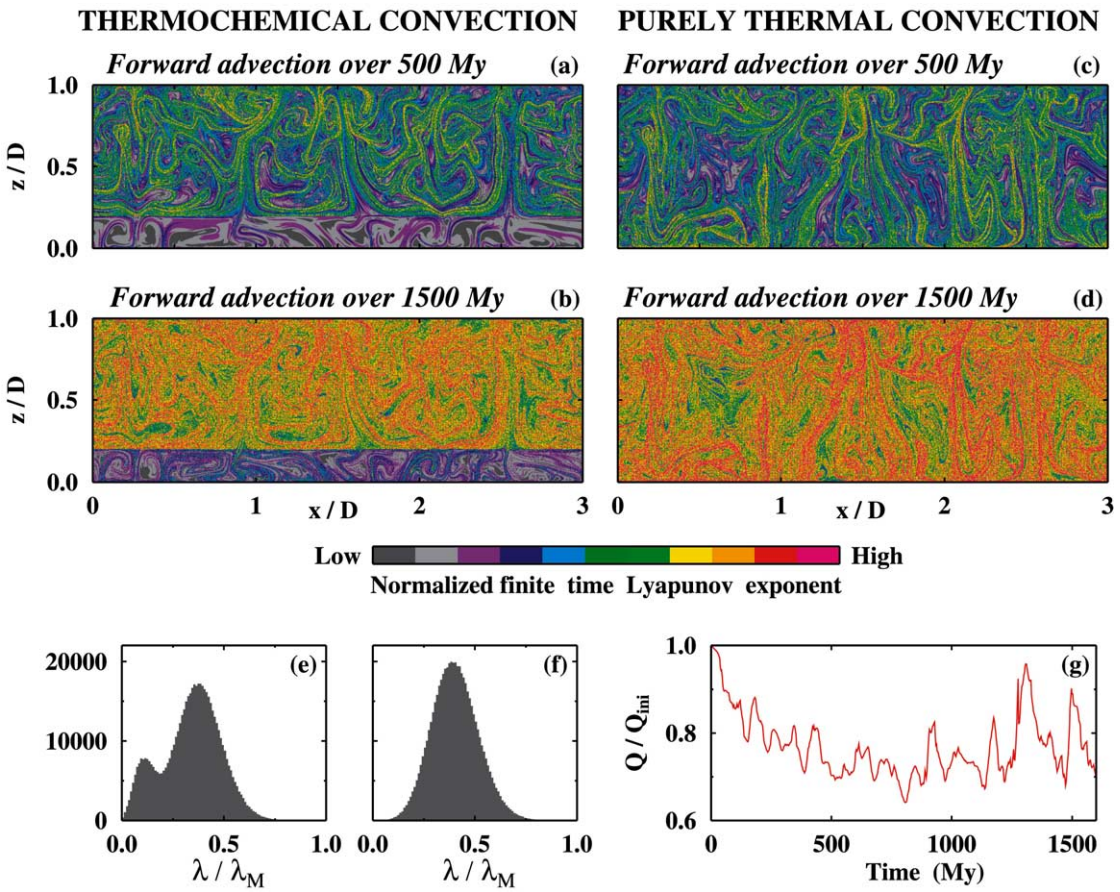


Fig. 6. Finite-time Lyapunov exponents. Thermochemical convection model, (a) forward advection for 500 Myr, (b) for 1500 Myr. Purely thermal convection model, (c) forward advection for 500 Myr, (d) for 1500 Myr. Color scheme as in previous figure. Tracers are in their initial location. Bottom: Histogram of Lyapunov exponent $\lambda$ normalized over the maximum value $\lambda_M$ after 1500 Myr, (e) for thermochemical model, (f) for purely thermal model. (g) Elapsed time vs. normalized surface heat flux for the thermochemical model.

is not surprising, since at this time the interface is not a complete barrier to the flow but allows for some mass exchange.

### 4.2. Methods based on Lyapunov exponent

The results of the finite-size Lyapunov exponent method (FSLE) are shown in Fig. 4, where we attribute to each tracer the value of the FSLE calculated for forward and backward advection over $\Delta T = 150$ Myr, using a growth factor $\gamma = 2$. This method shows very clearly regions with different stirring properties: inside the dense layer convection is sluggish and often the threshold distance ($\gamma\delta_0$) is not reached. On the contrary, the upper mantle is a region of high deformation and efficient stirring, where the threshold distance is rapidly attained. Although we present the results only for a given value of $\Delta T$ and $\gamma$ we verified that the results are robust also for a possible range of the growth factor and of the time interval. Clearly there is a trade-off between $\Delta T$ and $\gamma$: for a relatively short $\Delta T$ and a large $\gamma$, we will see only the fastest stretching regions, while in the rest of the domain the threshold distance will not be attained.

The results of the finite-time Lyapunov exponent method (FTLE) are shown in Fig. 5. Also in this case we attribute to each tracer the value of the FTLE calculated for forward and backward advection over $\Delta T = 150$ Myr. Tracers are in their initial location to facilitate the comparison with the previous figures. This method allows to visualize regions with different dynamical behavior: most of the deformations and stirring are localized in the mantle overlying the dense layer. Highly deformed material is associated with subduction zones, both in the upper mantle and at the boundary with the denser layer, where the subducted material folds. Within the dense layer the FTLE have the lowest values and the boundary between the two domains is clearly visible. For both backward advection panels (Fig. 5b and d) the ascending flow of plumes is characterized by fairly low values (violet–blue colors), which correspond well to the location of the stable material lines of Fig. 3b and d. With respect to previous methods the FTLE method seems to provide a detailed image of the stretching and folding events undergone by the fluid particles.

In Fig. 6 we show the FTLE for forward advection over two time intervals $\Delta T = 500$ Myr and $\Delta T = 1500$ Myr. For thermochemical convection (Fig. 6a and b) regions with different stirring properties can survive for long time periods: even after 1500 Myr tracers initially belonging to the dense layer still have relatively low FTLE and are clearly distinct from the overlying fluid which instead shows pronounced stirring. The bimodal distribution of the FTLE is also shown in the histograms (Fig. 6e), the lowest values characterize the denser layer. For purely thermal models (Fig. 6c and d) the FTLE indicate a fairly homogeneous stirring in the whole mantle, with only some 'islands' of less stirred material in the lower mantle. The corresponding histogram after 1500 Myr (Fig. 6f) shows a Gaussian shape.

Finally, for the thermochemical model we calculate the time evolution of the surface heat flux $Q$ normalized by the initial value $Q_{\mathrm{ini}}$. Fig. 6g shows that $Q/Q_{\mathrm{ini}}$ varies significantly with time, mainly due to hot plumes rising to the surface. This indicates that the advective component of heat transfer between the denser layer and the overlying fluid is important. Such result, even if preliminary, casts some doubts on the applicability of parametrized models at relatively low buoyancy numbers. Parametrized models in fact assume that the heat flux between the denser layer and the overlying fluid is entirely conductive, with the obvious consequence of a significant temperature increase in the denser layer [29].

## 5. Conclusions

The problem of characterizing mixing of a fluid flow is a difficult one. First of all, most of the geophysical flows are not periodic in time and the mathematical criteria necessary to describe mixing in aperiodic flows have been developed only in the last few years. Second, stretching of a fluid element results from the *history* of the strain along the trajectory [30], thus requiring the use of a Lagrangian description. However, connecting the Eulerian properties of a given velocity field to the Lagrangian properties of a trajectory is not an easy task [26]. In fact, even simple Eulerian velocity fields can generate unpredictable Lagrangian trajectories which may be indistinguishable from those obtained in a complex turbulent flow (see [26] and references therein).

Here we investigated three different Lagrangian techniques, requiring to compute the trajectories of more than half a million passive tracers forward and backward in time. We restricted our attention to two dynamical models and focussed on the model with a chemically denser layer at the base. This allowed us to test the ability of the Lagrangian techniques to detect the location of the dynamical barrier which inhibits mass exchanges and delimits domains characterized by different efficiency of stirring.

We found that Lyapunov exponents identify the sluggish denser layer by having the lowest finite-time Lyapunov exponents and the lowest finite-size Lyapunov exponents within the whole layer. Therefore, the location of the boundary between layers corresponds to the region of sharp contrast (i.e., high gradients) of Lyapunov exponent. The hyperbolic persistence time method in-

stead is able to detect the location of the boundary itself.

Methods based on the Lyapunov exponents clearly show the different dynamical behavior between the upper mantle and the underlying more viscous lower mantle. The upper mantle has the highest FSLE and FTLE (Figs. 4 and 5), indicating fast stretching rates and high deformations, mainly in subduction zones. The FTLE seem to be the best method to capture the fine structure of deformations induced by the flow. Since stirring results from the repeated action of stretching and folding, the distribution of FTLE provides a means to evaluate the efficiency of stirring.

The method based on the hyperbolic persistence time instead detects the skeleton of the main dynamical structures governing stirring. Forward calculations detect the location of the unstable (repelling) material lines, while backward calculations detect the location of stable (attracting) material lines. The features clearly shown are the subduction zones, also characterized by the highest strain rate-normalized hyperbolic persistence time, and the ascending plumes which form at the top of the denser layer.

Our results show that chemically heterogeneous material has a profound effect on stirring. We find well distinct FTLE between the dense layer and the overlying fluid either when we consider a finite-time interval (arbitrarily set at 150 Myr), or when we integrate forward in time for 1500 Myr. This indicates that denser material at the base of the Earth's mantle may remain distinct over long time periods. From a geochemical stand point this would imply that a distinct geochemical signature may develop, as shown by [31], or may be preserved, as shown by [21]. On the contrary, purely thermal models are more uniformly stirred, thus hampering the survival of distinct material, in agreement with previous results on mantle mixing.

We find that all of the Lagrangian techniques considered in our study provide a satisfactory description of the main structures governing stirring, and that they are able to evidence different and complementary aspects: the methods based on the Lyapunov exponents provide a clear picture of mantle domains characterized by different strength of stirring, while the method proposed by Haller identifies the skeleton of the main structures around which stirring is organized.

We are tempted to speculate that long lived geochemical heterogeneities may develop and survive only if the dynamics and stirring properties of the 'reservoirs' are distinct. In this respect chemically denser material may play an important role: it tends to segregate and it is entrained in form of filaments by mantle plumes. Therefore, the more heterogeneous geochemical signature of oceanic island basalts, with respect to mid-ocean ridge basalts may be largely due to incomplete stirring of entrained heterogeneous material.

We cannot speculate further about geochemical reservoirs, since in this study we did not calculate the time evolution of isotope ratios and element concentrations, as previously done by Samuel and Farnetani [21]. Moreover, our convection model has several simplifying assumptions: (i) We used a constant viscosity model which hinders the segregation of dense subducted crust [31]. (ii) We used a two-dimensional geometry. Although it is widely accepted that the third spatial dimension influences mixing, diverging conclusions have been drawn: according to Schmalzl et al. [32] mixing is reduced in 3-D, while for Ferrachat and Ricard [6] mixing is enhanced by surface toroidal forces, otherwise absent in 2-D. (iii) We modeled a Newtonian fluid. Non-Newtonian rheology would have been more appropriate for the mantle and it is expected to induce a less uniform deformation field, thus leading to the formation of regions with sharp differences in flow character [33].

Work is in progress to relax all of the above assumptions, with the objective to define the existence of geochemical reservoirs simultaneously under a dynamical point of view, by using the Lagrangian techniques described in this paper, and under a geochemical point of view, by following the evolution of element concentrations and isotope ratios.

## Acknowledgements

We thank the anonymous reviewer and M. Manga for their thorough reviews. We are grate-

ful to B. Legras for his constructive comments that improved the paper. We also wish to thank the lecturers of the summer school 'Dynamical barriers, stirring and mixing in geophysical flows – mathematical models and applications' (Cargese, France) for stimulating seminars. Calculations were conducted on the computers of IDRIS, which is kindly acknowledged. Figures were made with the General Mapping Tools (P. Wessel and W.H.F. Smith, EOS, Trans. AGU 76 (1995) 329).*[AC]*

## Appendix. Generalized criterion in the strain basis

The algorithm proposed by Haller [15] has two steps: First, calculating the maxima of hyperbolic persistence time along each Lagrangian trajectory, as explained in Section 3.1. Second, testing that the eigenvectors of $D_x u(\boldsymbol{x}(t),t)$ do not rotate too fast along the Lagrangian trajectory over the duration of hyperbolic persistence. In order to take into account the rotation of strain axis we follow the method by [25], which is a variant of the algorithm given by [17]. For each tracer trajectory we need to calculate the eigenvalues $\lambda$ of the strain rate tensor $\dot{\varepsilon}_{ij}$. Due to the incompressibility condition $\lambda_1 = -\lambda_2$. To each eigenvalue we associate a normalized eigenvector, for example, $\boldsymbol{e}_1 = (\cos\phi, \sin\phi)$ and $\boldsymbol{e}_2 = (-\sin\phi, \cos\phi)$. The rotation matrix $\boldsymbol{R} = [\boldsymbol{e}_1, \boldsymbol{e}_2]$ is defined in the orthonormal basis of the eigenvectors, $\boldsymbol{R}^{\mathrm{T}}$ is its transpose, and $\dot{\boldsymbol{R}}$ is its time derivative. As explained by [25] we need to calculate the sign of the determinant of:

$$\boldsymbol{R}^{\mathrm{T}} D_x u(\boldsymbol{x}(t), t)\boldsymbol{R} - \boldsymbol{R}^{\mathrm{T}}\dot{\boldsymbol{R}} \tag{15}$$

to obtain the new hyperbolic persistence time $d_T{}'^{+}$ and $d_T{}'^{-}$. The new hyperbolic persistence time field is shown for forward (Fig. 7a) and backward (Fig. 7b) advection only for the early stage. For comparison Fig. 7c and d show the hyperbolic persistence time field calculated by requiring only the first condition, as done in Section 3.1. (Note that the darker colors correspond to the tracers shown in Fig. 3a and b.) The region of high persistence time which marks the top of the denser layer (Fig. 7c and d) is absent in Fig. 7a and b, making the detection of the barrier more difficult.

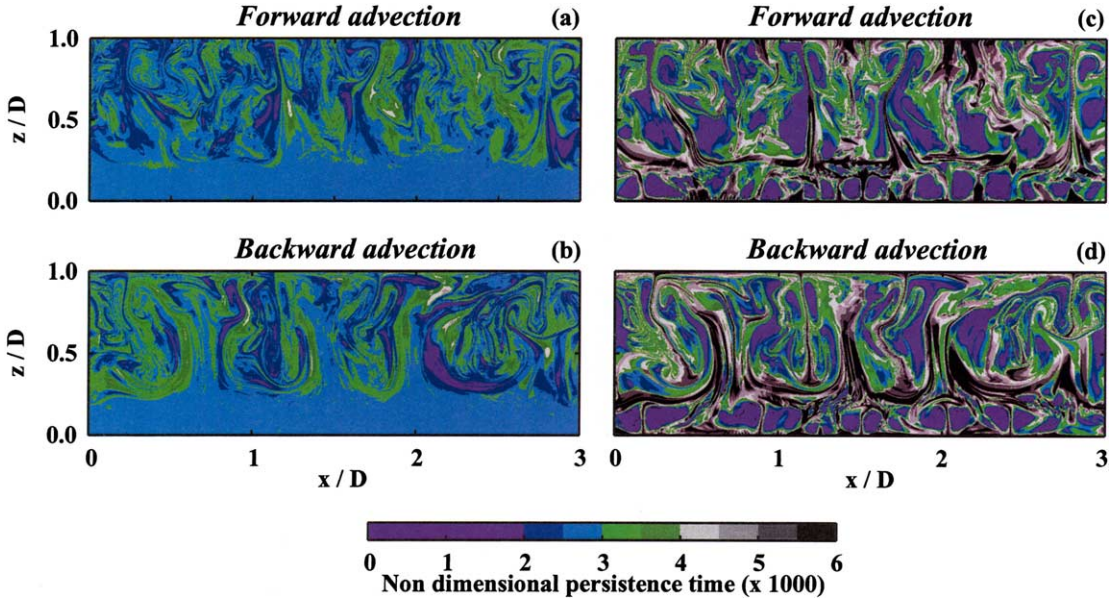


Fig. 7. Hyperbolic persistence time field. Left: Calculated with the condition on rotation given in the Appendix. Right: Calculated with the condition $\det D_x u < 0$. (a, c) Forward advection. (b, d) Backward advection.

## References


[1] N.R.A. Hoffman, D.P. McKenzie, The destruction of geochemical heterogeneities by differential fluid motions during mantle convection, Geophys. J. R. Astron. Soc. 82 (1985) 163–206.

[2] M. Gurnis, G.F. Davies, Mixing in numerical models of mantle convection incorporating plate kinematics, J. Geophys. Res. 91 (1986) 6375–6395.

[3] M. Gurnis, G.F. Davies, The effect of depth-dependent viscosity on convective mixing in the mantle and the possible survival of primitive mantle, Geophys. Res. Lett. 13 (1986) 541–544.

[4] U. Christensen, Mixing by time-dependent convection, Earth Planet. Sci. Lett. 95 (1989) 382–394.

[5] L.H. Kellogg, Mixing in the mantle, Annu. Rev. Earth Planet. Sci. 20 (1992) 365–388.

[6] S. Ferrachat, Y. Ricard, Regular vs. chaotic mantle mixing, Earth Planet. Sci. Lett. 155 (1998) 75–86.

[7] A. Zindler, S. Hart, Chemical geodynamics, Annu. Rev. Earth Planet. Sci. 14 (1986) 493–571.

[8] C.J. Allègre, B. Hamelin, A. Provost, B. Dupré, Topology in isotopic multispace and origin of mantle chemical heterogeneities, Earth Planet. Sci. Lett. 81 (1987) 319–337.

[9] S.R. Hart, E.H. Hauri, L.A. Oschmann, J.A. Whitehead, Mantle plumes and entrainment: isotopic evidence, Science 256 (1992) 517–520.

[10] T.-Y. Koh, B. Legras, Hyperbolic lines and the stratospheric polar vortex, Chaos 12 (2002) 382–394.

[11] B. Joseph, B. Legras, On the relation between kinematic boundaries, stirring, and barriers for the Antarctic polar vortex, J. Atmos. Sci., in press (2002).

[12] A.C. Poje, G. Haller, Geometry of cross-stream mixing in a double-gyre ocean model, J. Phys. Oceanogr. 29 (1999) 1649–1665.

[13] G.A. Voth, G. Haller, J.P. Gollub, Experimental measurements of stretching fields in fluid mixing, Phys. Rev. Lett. 88 (2002) 254501.

[14] J.M. Ottino, The Kinematics of Mixing: Stretching, Chaos and Transport, Cambridge University Press, Cambridge, 1989.

[15] G. Haller, Finding finite-time invariant manifolds in two-dimensional velocity fields, Chaos 10 (2000) 99–108.

[16] G. Haller, G. Yuan, Lagrangian coherent structures and mixing in two-dimensional turbulence, Physica D 147 (2000) 352–370.

[17] G. Haller, Lagrangian structures and the rate of strain in a partition of two-dimensional turbulence, Phys. Fluids 13 (2001) 3365–3385.

[18] G. Haller, Distinguished material surfaces and coherent structures in three-dimensional fluid flows, Physica D 149 (2001) 248–277.

[19] S.D. King, A. Raefsky, B.H. Hager, ConMan: vectorizing a finite element code for incompressible two-dimensional convection in Earth's mantle, Phys. Earth Planet. Inter. 59 (1990) 195–207.

[20] A. Chopleas, R. Boehler, Thermal expansivity in the lower mantle, Geophys. Res. Lett. 19 (1992) 1983–1986.

[21] H. Samuel, C.G. Farnetani, Thermochemical convection and helium concentrations in mantle plumes, Earth Planet. Sci. Lett. 207 (2003) in press.

[22] H. Akima, Algorithm 760: rectangular-grid-data surface fitting that has the accuracy of a bicubic polynomial, ACM Trans. Math. Soft. 22 (1996) 357–361.

[23] J.M. Ottino, C.W. Leong, H. Rising, P.D. Swanson, Morphological structures produced by mixing in chaotic flows, Nature 333 (1988) 419–425.

[24] A. Okubo, Horizontal dispersion of flotable particles in the vicinity of velocity singularity such as convergences, Deep-Sea Res. 17 (1970) 445–454.

[25] G. Lapeyre, B.L. Hua, B. Legras, Comments on 'Finding invariant manifolds in two-dimensional velocity fields', Chaos 11 (2001) 427–432.

[26] G. Boffetta, G. Lacorata, G. Redaelli, A. Vulpiani, Detecting barriers to transport: a review of different techniques, Physica D 159 (2001) 58–70.

[27] R.T. Pierrehumbert, Large-scale horizontal mixing in planetary atmospheres, Phys. Fluids A 2 (1991) 1250–1260.

[28] C.G. Farnetani, B. Legras, P.J. Tackley, Mixing and deformations in mantle plumes, Earth Planet. Sci. Lett. 196 (2002) 1–15.

[29] A.K. McNamara, P.E. van Keken, Cooling of the earth: a parametrized convection study of whole versus layered models, G3 1 (2000) 2000GC000045.

[30] G.K. Batchelor, The effect of homogeneous turbulence on material line surfaces, Proc. R. Soc. London A 213 (1952) 349–366.

[31] U. Christensen, A.W. Hofmann, Segregation of subducted oceanic crust in the convecting mantle, J. Geophys. Res. 99 (1994) 19867–19884.

[32] J. Schmalzl, G.A. Houseman, U. Hansen, Mixing in vigorous time-dependent three-dimensional convection and application to the Earth's mantle, J. Geophys. Res. 101 (1996) 21847–21858.

[33] A.A. Ten, Y.Y. Podladchikov, D.A. Yuen, T.B. Larsen, A.V. Malevsky, Comparison of mixing properties in convection with the particle-line method, Geophys. Res. Lett. 25 (1998) 3205–3208.